Stable SiOC/Sn Nanocomposite Anodes for Lithium-Ion Batteries with Outstanding Cycling Stability

Jan Kaspar, Caglar Terzioglu, Emanuel Ionescu, Magdalena Graczyk-Zajac, Stefania Hapis, Hans-Joachim Kleebe, and Ralf Riedel**

Silicon oxycarbide/tin nanocomposites (SiOC/Sn) are prepared by chemical modification of polysilsesquioxane Wacker-Belsil PMS MK ($SiOC_{MK}$) and polysiloxane Polyramic RD-684a ($SiOC_{RD}$) with tin(II)acetate and subsequent pyrolysis at 1000 °C. The obtained samples consist of an amorphous SiOC matrix and in-situ formed metallic Sn precipitates. Galvanostatic cycling of both composites demonstrate a first cycle reversible capacity of 566 $mAhg^{-1}$ for $SiOC_{MK}$/Sn and 651 $mAhg^{-1}$ for $SiOC_{RD}$/Sn. The superior cycling stability and rate capability of $SiOC_{RD}$/Sn as compared to $SiOC_{MK}$/Sn is attributed to the soft, carbon-rich SiOC matrix derived from the RD-684a polymer, which accommodates the Sn-related volume changes during Li-uptake and release. The poor cycling stability found for $SiOC_{MK}$/Sn relates to mechanical failure of the rather stiff and fragile, carbon-poor matrix produced from PMS MK. Incremental capacity measurements outline different final Li–Sn alloy stages, depending on the matrix. For $SiOC_{RD}$/Sn, alloying up to Li_7Sn_2 is registered, whereas for $SiOC_{MK}$/Sn $Li_{22}Sn_5$ stoichiometry is reached. The suppression of $Li_{22}Sn_5$ phase in $SiOC_{RD}$/Sn is rationalized by an expansion restriction of the matrix and thus prevention of a higher Li content in the alloy. For $SiOC_{MK}$/Sn on the contrary, the matrix severely ruptures, providing an unlimited free volume for expansion and thus formation of $Li_{22}Sn_5$ phase.

1. Introduction

Li-ion batteries represent the standard power source for portable electronics, such as mobile phones or laptop computers. The tremendous success of Li-ion secondary batteries started in 1991, when Sony Energytec introduced them into the market.[1,2] Since that time, cell design did not change significantly and the most common cell structure still consists of a carbon anode (e.g. graphite) in combination with a lithium metal oxide cathode (e.g. $LiCoO_2$). Over the years, power demands of new generation customer electronics steadily increased, pushing conventional cells to their limits. In addition, automobile industry strongly requests enhanced power supply for electrical and hybrid electrical driven vehicles. Thus, novel high power and high energy density materials are necessary in order to provide a sustainable future for Li-ion technology and to satisfy the emerging customer demands.[3–9]

Within this context, metals which can store lithium via alloying processes attracted attention as alternative anode material.[10–13] Lithium-tin alloy (Li-Sn) for instance has a theoretical capacity of 994 $mAhg^{-1}$ for its highest lithiation state of $Li_{22}Sn_5$, which is almost three times higher than that of the theoretical capacity of graphite (372 $mAhg^{-1}$). However, the major drawback related to tin-based anodes is their poor cycling stability, which emerges from large volume expansion and contraction during Li-uptake and release ($\Delta V \approx 260\%$ for Sn versus $Li_{22}Sn_5$).[14] Especially the tensile stress during contraction commonly initiates grain cracking and local grain pulverization. Consequently, electrical conduction pathways break down, causing capacity loss and poor cycle life time.[15,16]

Intense efforts were made in order to suppress this degradation by adopting nanostructured Sn-based architectures.[17–21] Sn-coated Cu-nanopillars for example, provide sufficient space to accommodate volume changes during the alloying/dealloying process, while demonstrating an enhanced cycle life.[19] However, such type of nano-architectures exhibit low energy density due to a rather low active mass-to-volume ratio. The major drawback related to Sn-nanoparticles is the loss of their initial morphology upon cycling. In consequence, the beneficial properties of the initial nanoscale get lost, including enhanced mechanical integrity towards crack initiation and pulverization.[10,11]

Another approach to prepare Sn-based electrodes with improved cycle stability was demonstrated by Derrien et al., who synthesized Sn/C nanocomposites by embedding Sn nanoparticles into a carbon matrix.[17,21] As the Sn particles are well distributed throughout the matrix, the initial microstructure remains stable during long term cycling. Additionally, the carbon matrix increases the electrical conductivity and ensures electrical wiring, even when cracking and pulverization occur.

J. Kaspar, C. Terzioglu, Dr. E. Ionescu,
Dr. M. Graczyk-Zajac, Prof. R. Riedel
Institut für Materialwissenschaft
Technische Universität Darmstadt
Jovanka Bontschits Straße 2, 64287 Darmstadt
E-mail: kaspar@materials.tu-darmstadt.de;
riedel@materials.tu-darmstadt.de
S. Hapis, Prof. H.-J. Kleebe
Institut für Angewandte Geowissenschaften
Technische Universität Darmstadt
Schnittspahnstraße 9, 64287 Darmstadt

DOI: 10.1002/adfm.201303828

In the present work, the direct synthesis of novel ceramic/tin nanocomposites was achieved by an innovative single-source-precursor approach. Accordingly, polyorganosiloxanes modified with tin(II)acetate were prepared and thermally converted into SiOC/Sn nanocomposites at 1000 °C. Two different commercially available polysiloxanes were used for the modification, namely *i)* polysilsesquioxane Wacker-Belsil PMS MK, which transforms into a silicon oxycarbide matrix ($SiOC_{MK}$) with moderate free carbon content (≈6 wt%) and a Young's modulus of 85–96 GPa and *ii)* polysiloxane Polyramic RD-684a, which converts into a carbon-rich (≈41 wt% free carbon) silicon oxycarbide matrix ($SiOC_{RD}$) with a consequently lower value of the Young's modus of 66 GPa.[22–26] Interestingly, the electrochemical performance of the SiOC/Sn-based nanocomposites prepared within the present study correlates with the phase composition and the stiffness of the silicon oxycarbide matrices. The carbon-poor and stiff matrix (as for $SiOC_{MK}$) is found to not be able to withstand volume changes related to Li-Sn alloying, since a serious damage of the electrodes has been monitored, accompanied by a strong capacity fading. If the matrix is carbon-rich and soft (as for $SiOC_{RD}$), it is able to accommodate the high volume expansion upon alloy formation and thus prevents the electrode failure.

2. Results and Discussion

2.1. Materials Characterization

The pure polysiloxanes PMS MK and RD-684a as well as the $Sn(ac)_2$-modified polymers were investigated by FTIR spectroscopy (**Figure 1** and **Figure 2**).

The spectrum of PMS MK shows absorption bands at ν = 590 cm^{-1} (SiOC-H), ν = 768, 1278 cm^{-1} (Si-CH_3), ν = 1030 cm^{-1} (Si-O-C) and ν = 1122 cm^{-1} (Si-O-Si), as previously reported.[27–31] The FTIR spectrum of the $Sn(ac)_2$-modified sample shows additional absorption bands corresponding to the acetate ligands, i.e. ν = 1340, 1572 cm^{-1} (C-O), ν = 1385 ($C\text{-}CH_3$) and ν = 1524 cm^{-1} (C=C).[32–34] Furthermore, two new absorption bands were assigned at ν = 689 cm^{-1} (Sn-O)[35,36] and ν = 925 cm^{-1} (Si-O-Sn).[37] Thus, the added $Sn(ac)_2$ undergoes a reaction with the Si-OH reactive groups present in PMS MK (**Figure 3**), upon release of acetic acid and the formation of Si-O-Sn units. The formation of Si-O-M (M = metal) units upon modification of the polymer with metal alkoxides, as well as with acetylacetonates and acetates, was demonstrated previously for metalorganic precursors of other metals, e.g. Fe,[27] Zr[28] and Hf.[29,30]

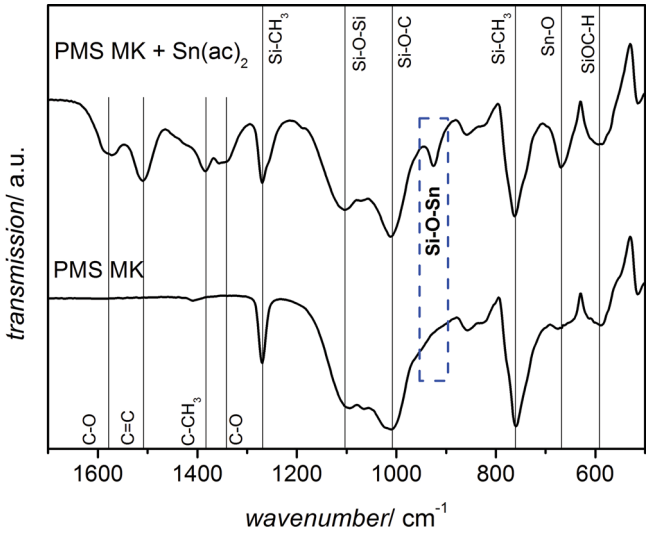

Figure 1. FTIR spectra of PMS MK and $Sn(ac)_2$ modified PMS MK.

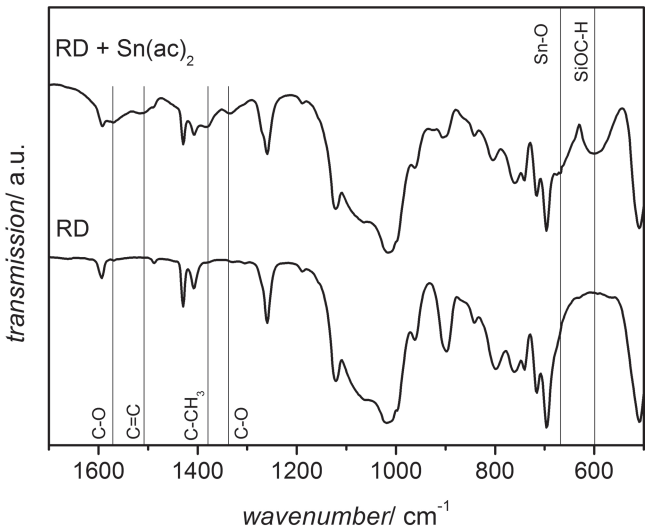

Figure 2. FTIR spectra of RD-684a and $Sn(ac)_2$ modified RD-684a.

The spectra of RD-684a and $Sn(ac)_2$-modified RD-684a (Figure 2) look very similar. Within the polymer there are neither OH nor Si-OR groups to react with $Sn(ac)_2$ as it is the case for

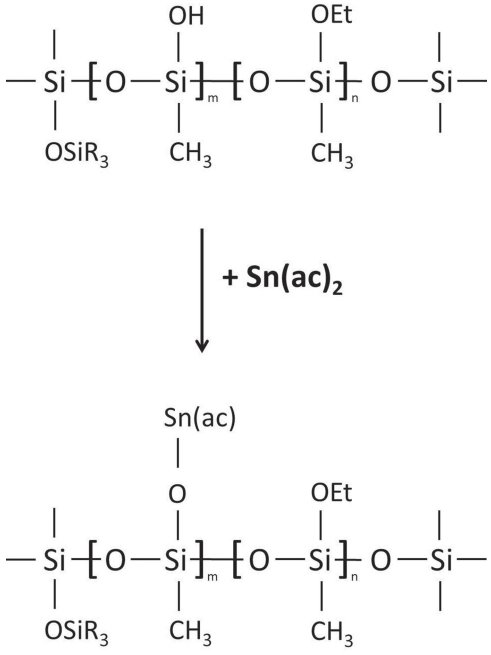

Figure 3. Chemical modification of PMS MK with $Sn(ac)_2$.

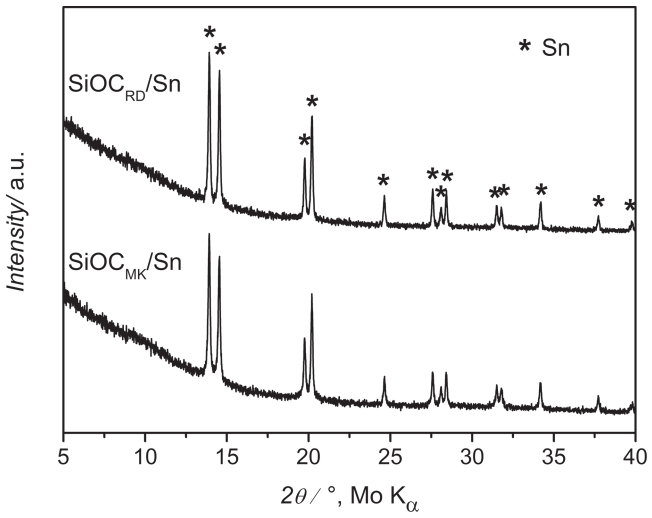

Figure 4. XRD patterns of SiOC$_{MK}$/Sn and SiOC$_{RD}$/Sn after pyrolysis at 1000 °C.

PMS MK. One could expect a reaction of Si-H with $Sn(ac)_2$ upon the formation of Si-Sn units, as it is reported for the reaction of polycarbosilanes with acetylacetonates by Ishikawa et al.[38] and shortly discussed by Ionescu et al.[39] However, the formation of Si-metal units still needs direct proof and thus no Si-Sn vibration could be assigned in the FTIR spectrum of the modified sample. Similar to PMS MK, the spectrum of modified RD-684a exhibits additional absorption bands related to the acetate ligands: ν = 1339, 1570 cm^{-1} (C-O), ν = 1380 cm^{-1} (C-CH$_3$) and ν = 1514 cm^{-1} (C=C) and at ν = 600 cm^{-1} (SiOC-H) and at ν = 667 cm^{-1} (Sn-O).[31–36] Although the exact reaction mechanism between $Sn(ac)_2$ and polysiloxane RD-684a remains unclear, the important finding here is that the transformation of the modified polymer into a SiOC/Sn composite occurs comparable to that of the $Sn(ac)_2$-modified PMS MK.

The X-ray diffraction patterns of SiOC$_{MK}$/Sn and SiOC$_{RD}$/Sn are shown in **Figure 4**. Both ternary silicon oxycarbides are found to be fully X-ray amorphous as previously reported,[22,25,28] whereas the Sn-modified samples exhibit the presence of metallic tin, formed in-situ upon pyrolysis. TEM analysis of both nanocomposites (**Figure 5** and **Figure 6**) illustrates the presence of spherical crystalline Sn inclusions within the amorphous matrices. In the case of SiOC$_{MK}$/Sn (Figure 5) a large number of homogeneously dispersed, ultrafine Sn grains with size below 10 nm and a few ones with larger size that tend to agglomerate are found. For SiOC$_{RD}$/Sn (Figure 6), Sn precipitations with an average diameter of 45 nm are observed, likewise homogeneously distributed throughout the SiOC matrix. In addition a very few ones with lager diameter are present as well. For both composites, the EDS inset in the high resolution micrographs outlines the amorphous matrices as composed of Si, O and C. The Cu-signal originates from the support grid. The round-shaped Sn particles in both nanocomposites indicate that liquid tin shows a poor wettability for the SiOC matrix, as it is known for ceramics with covalent bonding.[40,41] Similar features were recently found in the case of SiCN/Fe-based nanocomposites, which exhibited spherical-shaped Fe_5Si_3 precipitates dispersed within a SiCN matrix.[39,42]

Interestingly, the crystallization of tin oxide was not found upon pyrolysis of the modified precursors, unlike in other cases, where the modification of polysiloxanes with metal alkoxides, acetylacetonates or acetates was shown to lead to a precipitation and crystallization of the corresponding metal oxides, i.e. to the formation of SiOC/MO$_x$ nanocomposites (M = Al,[31] Ti,[43] Zr,[28] Hf,[29,30] Nb,[44] Ta,[44,45] Mn and Lu,[27] Gd[46]). However, in all cases a similar behavior with respect to the polymer-to-ceramic transformation is expected, which leads in a first step to single phase-amorphous SiMOC intermediates, subsequently partitioning into amorphous SiOC/MO$_x$. Recently we have shown that the phase composition and crystallization of those SiOC/MO$_x$ ceramics strongly depend on the redox stability of the metal oxide towards the C-CO system.[27] As in the investigated

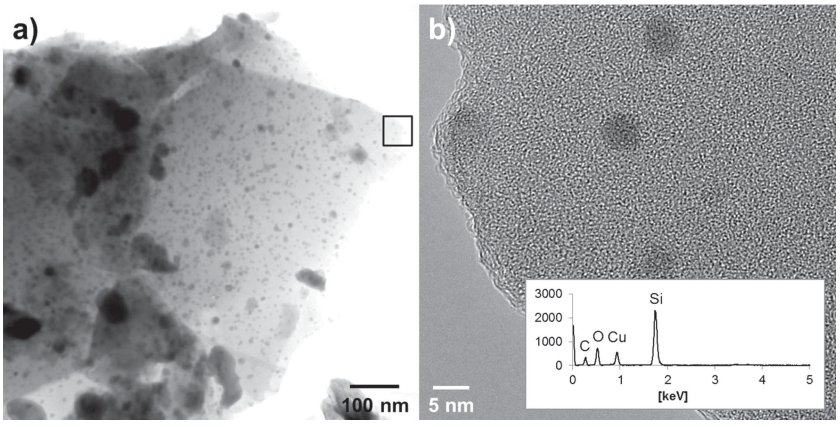

Figure 5. a) TEM micrograph of SiOC$_{MK}$/Sn and b) high-resolution image with EDS pattern of the amorphous SiOC matrix.

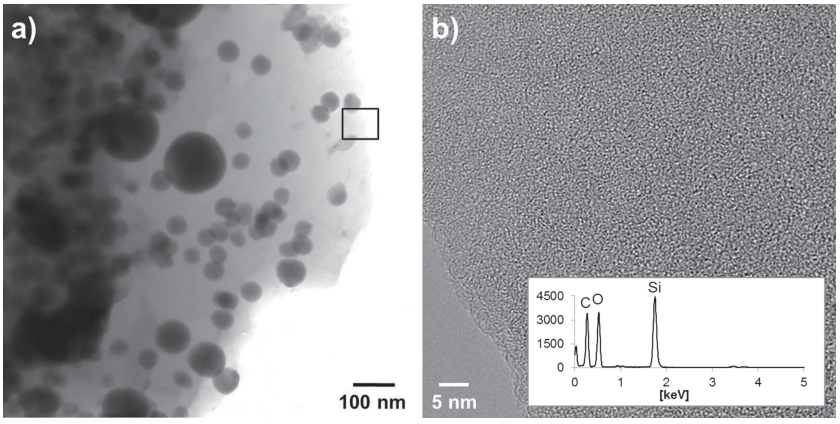

Figure 6. a) TEM micrograph of SiOC$_{RD}$/Sn and b) high-resolution image with EDS pattern of the amorphous SiOC matrix.

Table 1. Elemental analysis data and chemical formulae of $SiOC_{MK/RD}$/Sn, $SiOC_{MK/RD}$ matrices and $SiOC_{MK/RD}$ references. The weight fractions of silicon carbide, silica and segregated carbon were quantified according to the literature.[47]

Sample	Si [wt%]	O [wt%]	C [wt%]	Sn [wt%]	Chemical Formula (normalized to 1 Si)	SiC [wt%]	SiO_2 [wt%]	Free C [wt%]	Sn [wt%]
$SiOC_{MK}$/Sn	34.54	36.04	8.42	21.0	$SiO_{1.83}C_{0.57}Sn_{0.14}$ $(SiO_{1.83}C_{0.08})Sn_{0.14}$ + 0.49C	4.15	67.67	7.18	21.0
$SiOC_{MK}$ – matrix	43.72	45.62	10.66	–	$SiO_{1.83}C_{0.57}$ $SiO_{1.83}C_{0.08}$ + 0.49C	5.25	85.66	9.09	–
$SiOC_{MK}$[a)]	48.68	39.77	11.55	–	$SiO_{1.43}C_{0.55}$ $SiO_{1.43}C_{0.28}$ + 0.27C	19.66	74.68	5.66	–
$SiOC_{RD}$/Sn	24.44	23.85	26.01	25.7	$SiO_{1.71}C_{2.49}Sn_{0.25}$ $(SiO_{1.71}C_{0.14})Sn_{0.25}$ + 2.35C	5.01	44.78	24.51	25.7
$SiOC_{RD}$ – matrix	30.94	30.19	32.92	–	$SiO_{1.71}C_{2.49}$ $SiO_{1.71}C_{0.14}$ + 2.35C	6.34	56.69	31.02	–
$SiOC_{RD}$[a)]	31.76	21.42	46.82	–	$SiO_{1.18}C_{3.45}$ $SiO_{1.18}C_{0.41}$ + 3.04C	18.50	40.22	41.28	–

[a)]Reference data added for comparison.

systems carbon is found to be present in excess, the relative stability of the systems C-CO and M-MO_x determine the phase composition and the crystallization of these SiMOC materials. Zirconia, hafnia or gadolinia are stable with respect to their carbothermal reduction to metallic elements, whereas tin oxide, which is assumed to be generated intermediary upon pyrolysis of the tin acetate-modified polysiloxanes, is not stable under carburizing conditions. As tin does not form any silicides or carbides, the formation of SiOC/Sn nanocomposites is consequently related to the carbothermal reduction of SnO to Sn.

Table 1 presents the chemical composition of the tin comprising composites, their ceramic matrices and pure $SiOC_{MK/RD}$ as reference. The chemical formula of the compounds normalized to silicon and the derived phase composition in terms of silicon carbide, silica and free C, quantified according to the literature,[47] are included.

For both composites, it is evident that the total amount of carbon within the matrix is reduced upon Sn incorporation. For $SiOC_{MK}$(/Sn) it decreases from 11.55 to 10.66 wt% and for $SiOC_{RD}$(/Sn) from 46.82 to 32.92 wt%. This effect of the modification of polysiloxanes and polysilazanes with metal organic precursors has been previously reported and shown to significantly affect the microstructure and physical properties of the resulting nanocomposites.[27–29,31,48] Interestingly, the amount of free carbon in $SiOC_{MK}$/Sn (9.09 wt%) is higher than that of the reference sample $SiOC_{MK}$ (5.66 wt%), despite the overall content of carbon decreases upon modification. On the contrary, for carbon-rich $SiOC_{RD}$(/Sn) the content of free carbon decreases from 41.28 to 31.02 wt%, following the tendency of the total carbon content.

2.2. Electrochemical Results

Electrodes prepared from the composites were cycled by PCGA protocol in order to follow the incremental capacity as a function of the lithiation/delithiation potential and to trace the electrochemical activity of the embedded tin. Differential capacity plots for the first, second and fifth cycles are shown in **Figure 7**. For both samples, in the cathodic branch cycle two and five, strong and characteristic signals for Li-Sn alloying are visible: For $SiOC_{MK}$/Sn at 0.64 V (LiSn) and 0.38 V ($Li_{22}Sn_5$) and for $SiOC_{RD}$/Sn at 0.66 V (LiSn) and 0.42 V (Li_7Sn_2).[14] The presence of these signals reveals the electrochemical activity of the tin phase. Note that there is a distinct difference in the detected final alloy stage between $SiOC_{MK}$/Sn and $SiOC_{RD}$/Sn. For $SiOC_{MK}$/Sn the highest alloy phase $Li_{22}Sn_5$ is reached, whereas for $SiOC_{RD}$/Sn alloying stops with Li_7Sn_2. In the anodic branches, several signals for Li-Sn dealloying appear around 0.44, 0.60, 0.61, 0.70 and 0.78 V. The numerous anodic peaks indicate that dealloying occurs via multifold reactions and stages and cannot simply be considered as the reverse reaction-path of the observed alloying process.[14]

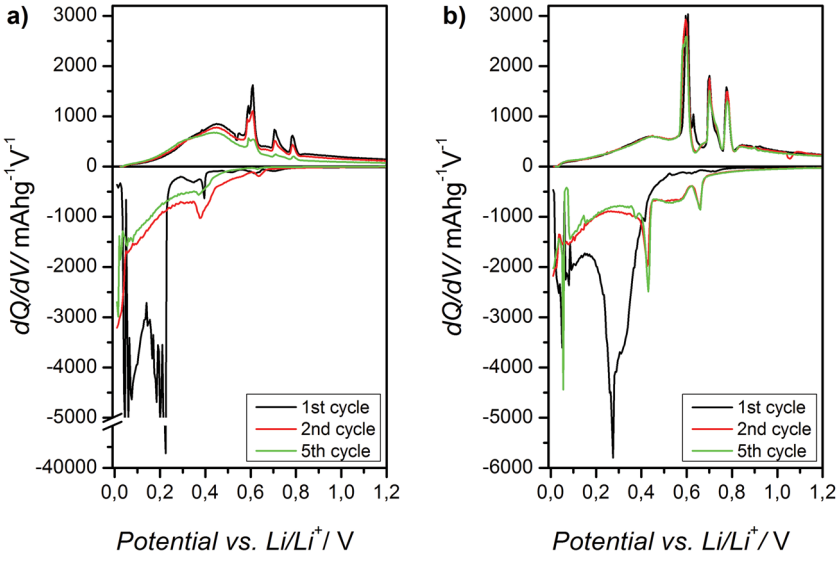

Figure 7. Differential capacity plot for a) $SiOC_{MK}$/Sn and b) $SiOC_{RD}$/Sn; first, second and fifth cycle are shown.

Table 2. Overview of the first cycle charging, discharging and irreversible capacity and coulombic efficiency (η) for $SiOC_{MK/RD}$/Sn and pure $SiOC_{MK/RD}$ reference electrodes.

	C_{ch} [$mAhg^{-1}$]	C_{dis} [$mAhg^{-1}$]	C_{irr} [$mAhg^{-1}$]	η [%]
$SiOC_{MK}$[a)]	1097	236	861	22
$SiOC_{MK}$/Sn	1190	566	624	48
$SiOC_{RD}$[a)]	978	598	380	61
$SiOC_{RD}$/Sn	1022	651	371	64

[a)]Reference electrodes were prepared and cycled similar to the composites.

The suppression of the formation of $Li_{22}Sn_5$ in the $SiOC_{RD}$/Sn composite is related to the restriction of the alloy expansion within the embedding matrix. The volume increase for Li_7Sn_2 only amounts 75%, as compared to $Li_{22}Sn_5$ resulting in less mechanical stress transference to the matrix. This lower load can be well accommodated by the soft $SiOC_{RD}$ without degradation. The stiff and fragile $SiOC_{MK}$ on the contrary, is not able to withstand the alloy expansion and thus ruptures and pulverizes during cycling. Consequently, a considerably higher volume is available for the Li-Sn expansion and the highest known Li-Sn stoichiometry $Li_{22}Sn_5$ is finally formed.

From the elemental analysis data (Table 1), a theoretical capacity for the $SiOC_{MK}$/Sn and $SiOC_{RD}$/Sn composites can be calculated, taking the mass ratio SiOC:Sn into account. For the sample $SiOC_{MK}$/Sn, the theoretical capacity of $Li_{22}Sn_5$ (994 $mAhg^{-1}$) and for $SiOC_{RD}$/Sn that of Li_7Sn_2 (790 $mAhg^{-1}$) is considered. The capacity contribution of the SiOC matrices is estimated from the reference electrode data (**Table 2**). Accordingly, the expected capacities for the composites amount 395 $mAhg^{-1}$ ($SiOC_{MK}$/Sn) and 647 $mAhg^{-1}$ ($SiOC_{RD}$/Sn). For $SiOC_{RD}$/Sn the estimation is in excellent agreement with the experimentally registered value of 651 $mAhg^{-1}$. The experimentally found higher capacity of $SiOC_{MK}$/Sn (566 $mAhg^{-1}$) can be explained by two factors: Firstly, for the calculation of the theoretical capacity of $SiOC_{MK}$/Sn composite the data found for pure $SiOC_{MK}$ was applied. However, the presence of dispersed metallic tin nanoparticles might increase the electronic conductivity and/or the availability of carbon phase within the SiOC matrix and thus increases the composite capacity in a non-linear way with respect to the calculation. A similar phenomenon was reported for mixtures of carbon-poor SiCN ceramic and graphite.[49,50] In addition the free carbon content in the sample was found slightly enhanced, providing additional Li-ion storing sites. Secondly, the higher capacity can be attributed to the partially reversible storage of less-ionic lithium species in micropores[51] as well as in the vicinity of SiO_4 units.[52] These reactions take place at the potential E < 0.1 V giving a well pronounced peak (c.f. Figure 7a)). The lithium storage in places close to the oxygen is most probably responsible for the high first lithiation capacity (1190 $mAhg^{-1}$) but due to a strong interaction between lithium and oxygen it brings about a poor reversibility.

Figure 8 and **Figure 9** present the galvanostatic cycling (GCPL) performance of the composites at different current rates and illustrate their cycling stability. Table 2 summarizes the first cycle charge (C_{ch}), discharge (C_{dis}) and irreversible capacity (C_{irr}), as well as the columbic efficiency (η) of the first cycle; η denoting the charge ratio $C_{ch}/C_{dis} \times 100\%$ and quantifying the amount of charge recovered within one cycle.

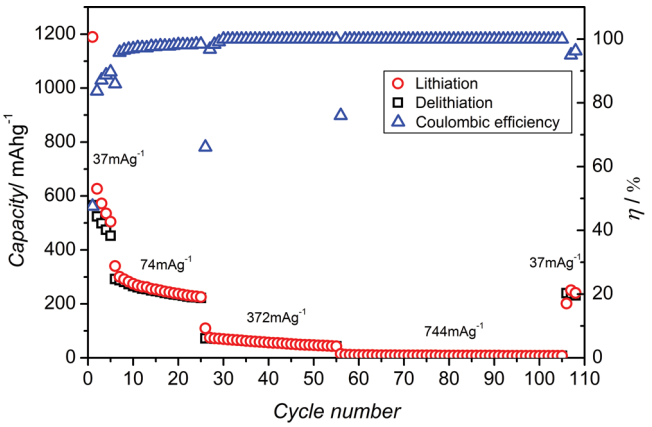

Figure 8. Capacity performance and coulombic efficiency (η) of $SiOC_{MK}$/Sn at different current rates: 5 × 37 mAg^{-1}, 20 × 74 mAg^{-1}, 30 × 372 mAg^{-1}, 50 × 744 mAg^{-1} and 3 × 37 mAg^{-1}.

For $SiOC_{MK}$/Sn, the initial lithiation capacity amounts 1190 $mAhg^{-1}$, while 566 $mAhg^{-1}$ are recovered during the first extraction, with a coulombic efficiency of 48%. $SiOC_{RD}$/Sn on the contrary provides a lower first cycle lithation of 1022 $mAhg^{-1}$, but 651 $mAhg^{-1}$ are recovered reversibly, with a significant higher coulombic efficiency of 64%.

The PMS MK-based sample demonstrates a poor cycling stability and continuous capacity fading at all current rates. When increasing the cycling current to 74 mAg^{-1} the capacity drops to 293 $mAhg^{-1}$ and further decreases to 222 $mAhg^{-1}$ within subsequent 20 cycles. At high current (744 mAg^{-1}) almost no electrochemical activity is found. The coulombic efficiency of cycle one to five does not exceed 90%, confirming irreversible losses, caused by two interplaying processes. Firstly, the continuous solid electrolyte interface formation, since new surface is steadily created when the electrode particles crack during Li uptake and release. Secondly, the irreversible Li-ion capture within once broken and electrically insolated grains in the electrode. SEM micrographs of $SiOC_{MK}$/Sn

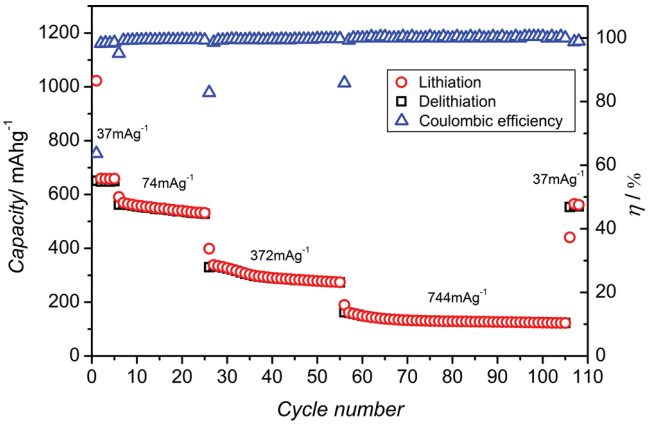

Figure 9. Capacity performance and coulombic efficiency (η) of $SiOC_{RD}$/Sn at different current rates: 5 × 37 mAg^{-1}, 20 × 74 mAg^{-1}, 30 × 372 mAg^{-1}, 50 × 744 mAg^{-1} and 3 × 37 mAg^{-1}.

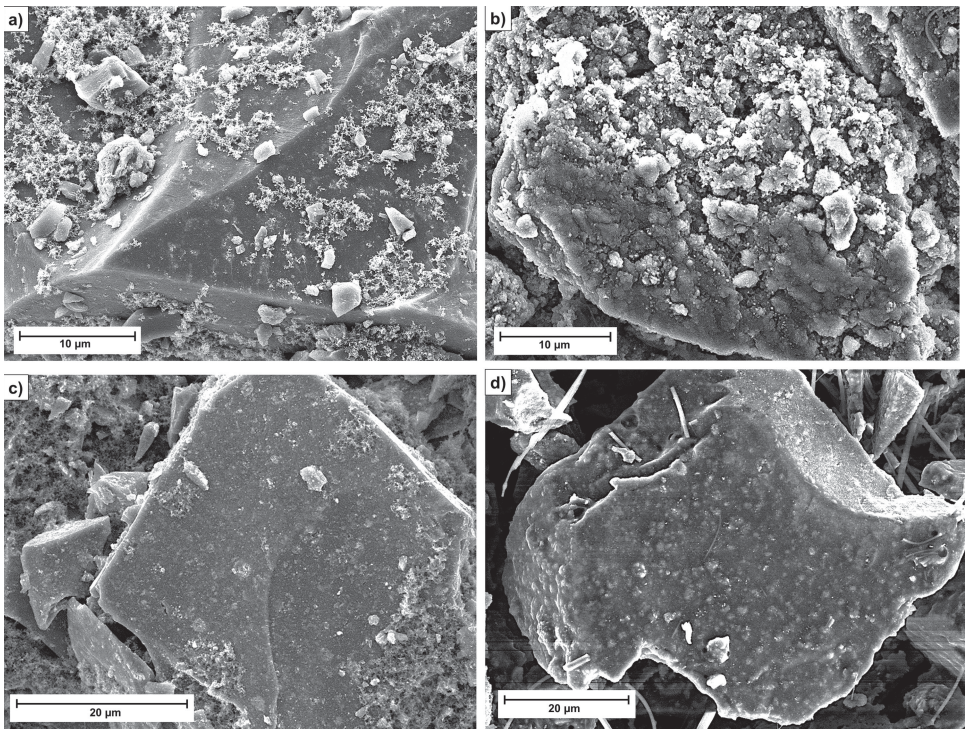

Figure 10. SEM image of a) $SiOC_{MK}$/Sn electrode before cycling, b) after 108 cycles; c) $SiOC_{RD}$/Sn electrode before cycling, d) after 108 cycles (the fibers represent remaining rests of separator).

before and after cycling (**Figure 10**) illustrate this degradation process.

For $SiOC_{RD}$/Sn on the contrary, the reversible capacity remains stable with 651 $mAhg^{-1}$ during continuous charging/discharging with 37 $mAhg^{-1}$. At a current rate of 74 mAg^{-1}, the registered capacity reduces to 562 $mAhg^{-1}$, showing little fading over the 20 measured cycles; in average ~1.5 $mAhg^{-1}$ are lost in each cycle. Even at high current of 744 mAg^{-1} a significant electrochemical activity is still detected for $SiOC_{RD}$/Sn, with an average reversible capacity of 133 $mAhg^{-1}$. When low currents are re-applied at the end of high current series, 562 $mAhg^{-1}$ are recovered for $SiOC_{RD}$/Sn, while for $SiOC_{MK}$/Sn only 232 $mAhg^{-1}$ could be realized.

We explain the superior cycling stability of the $SiOC_{RD}$/Sn sample by its beneficial matrix properties. $SiOC_{RD}$ represents a soft (E = 66 GPa,[25] electrochemically active ceramic with an intrinsically high content of free carbon (>41 wt%).[22–24] Scarmi et al.[53] presented the model structures of carbon-poor and carbon-rich SiOC amorphous ceramics. According to their model, carbon-poor SiOC materials are represented as nanodomains of sp^2 carbon, discontinuously dispersed in silica. Carbon-rich SiOC on the contrary, consists of a cellular network of graphene sheets of sp^2 carbon, where nanodomains of silica are sequestered within cells created by the graphene sheets. Accordingly, the graphene-like network can accommodate the volume change of the Sn nanoparticles upon Li-alloying/dealloying, as it can elastically deform. Consequently, the volume expansion of Sn does not lead to matrix rupture for the $SiOC_{RD}$/Sn composite. In the case of low-carbon $SiOC_{MK}$/Sn, the induced stresses upon Li-Sn alloy expansion exceed the critical fracture strength of the matrix. Cracks evolve and irreversibly damage the stiff and fragile ceramic, with the result of failure. SEM micrographs of cycled electrodes illustrate this feature, revealing cracking and partially pulverized composite-grains for $SiOC_{MK}$/Sn, whereas for $SiOC_{RD}$/Sn almost no degradation is observed (Figure 10).

3. Conclusion

A new method of preparation of SiOC/Sn composite materials with outstanding stability during electrochemical insertion and extraction of lithium ions is presented. The SiOC/Sn nanocomposites were synthesized via pyrolysis of the polysiloxanes PMS MK and RD-684a modified with tin(II)acetate at 1000 °C. Upon pyrolysis, metallic Sn segregates within the SiOC ceramics, forming spherical nanoparticles of different sizes. In the case of modified PMS MK, the composite predominantly contains Sn inclusions below 10 nm, whereas for modified RD-684a an average grain diameter of around 45 nm is found. Electrochemical measurements reveal a superior performance and cycling stability of the carbon-rich and therefore rather soft $SiOC_{RD}$/Sn material (C_{max} = 651 $mAhg^{-1}$ and stable), while fast capacity fading is registered for the carbon-poor and therefore stiff and fragile $SiOC_{MK}$/Sn composite (C_{max} = 566 $mAhg^{-1}$, not stable). Incremental capacity measurements outlined different final lithium-tin alloy stages, strongly depending on the embedding matrix and its properties. $Li_{22}Sn_5$ and Li_7Sn_2 are formed in $SiOC_{MK}$/Sn and $SiOC_{RD}$/Sn, respectively. Our study emphasizes that a single-source-precursor approach has two crucial advantages for synthesizing Sn-containing nanocomposites as high-performance material for Li-ion battery anode application:

i) it provides the in-situ generation of Sn nanoparticles homogeneously dispersed within the SiOC host and *ii)* the choice of suitable single-source-precursors allows for tailoring of the matrix properties (i.e. carbon-content/stress compliance), to be able to withstand the volume expansion of the Sn precipitates upon alloying with Li.

4. Experimental Section

Materials Synthesis: The synthesis of the single-source precursors was performed upon chemical modification of polysilsesquioxane PMS MK (Wacker-Belsil, Germany) and polysiloxane Polyramic RD-684a (Starfire Systems Inc., USA) with tin(II)acetate ($Sn(ac)_2$, Sigma-Aldrich, Germany). Both reactants were dissolved in xylene and mixed and stirred for several hours for reaction. The solvent was removed and the obtained powders were dried in vacuum (10^{-2} mbar). The ratio $Sn(ac)_2$ to polymer was adjusted to 1:1.5 by weight for $Sn(ac)_2$:PMS MK and 1:2 for $Sn(ac)_2$:RD-684a, in order to achieve comparable tin contents in the SiOC/Sn nano-composites after pyrolysis. The thermal conversion of the single-source precursors was performed in a two-step procedure in a horizontal alumina tube furnace under argon atmosphere: Cross-linking at 250 °C (50 °C h^{-1}; 2 h) followed by subsequent pyrolysis at 1000 °C (100 °C h^{-1}; 3 h).

Characterization Methods: FTIR spectra were collected using a Bruker Vertex 70 FT-IR instrument (Bruker, USA) in attenuated total reflectance geometry. X-ray diffraction (XRD) measurements were performed at a STOE X-ray diffractometer (Stoe & Cie GmbH, Germany) in transmission geometry (Mo K_α radiation). For elemental analysis, a carbon analyzer Leco-200 (Leco Corporation, USA) was used to determine the carbon content and an N/O analyzer Leco TC-436 (Leco Corporation, USA) to determine the corresponding oxygen content. The tin content was measured at "Mikroanalytisches Labor Pascher" (Remagen-Bandorf, Germany) by inductively coupled plasma atomic emission spectroscopy (ICP-AES). The silicon fraction was calculated as the difference to 100 wt% of the sum of the wt% values of carbon, oxygen and tin, assuming no other elements being present in the samples. Scanning electron microscopy (SEM) images of uncycled and cycled electrodes were recorded with a Philips XL30 FEG (FEI, Netherlands). Transmission electron microscopy (TEM) studies on powder samples, dispersed on a lacy carbon Cu-grid, were performed, utilizing a JEOL 2100F instrument (JEOL, Japan) operated at 200 keV. An energy-dispersive X-ray detector XMAX-80 (Oxford Instruments, UK), attached to the instrument, was used for the local chemical analysis.

Electrode Preparation: For electrochemical testing, the pyrolyzed powders (active mass) were ground and mixed with Carbon Black Super P (Timcal Ltd., Switzerland) as conducting additive and polyvinylidene fluoride binder (Solvay S.A., Germany) solved in *n*-methyl-2-pyrolidone (NMP, BASF, Germany) in the weight ratio 85:5:10. The mixture was homogenized and tape casted on the rough side of a 10 µm thin copper foil (SE-Cu58, Schlenk Metallfolien GmbH & Co KG, Germany). The tape (wet-film thickness 150 µm) was dried at 80 °C for several hours in order to remove the solvent NMP. The film thickness after drying was about 80 µm, with an average load of 4.5 mg cm^{-2}. Electrodes of 7 mm in diameter were cut and vacuum-dried at 80 °C for 24 h, before transferred to an argon-filled glove box for cell assembly. Two electrode Swagelok type cells were used, with metallic lithium (Li-tape 99.9% purity, 0.75 mm thickness, Alfa Aesar, UK) as reference and counter electrode, 1 M $LiPF_6$ solved in EC:DMC, ratio 1:1 (LP30, Merck KGaA, Germany) as electrolyte and Whatman glass fiber filter (Whatman, UK) as separator. The prepared hermetic cells were connected to a VMP multipotentiostat (BioLogic, France) and studied by Potentiodynamic Cycling with Galvanostatic Acceleration (PCGA) in order to assess the incremental capacity as a function of lithiation/delithiation potential. The potential window was set to 2.5–0.005 V (E vs. Li/Li^+) with scanning steps of 50 mV and a limiting current of 37 mAg^{-1}. Galvanostatic Cycling with Potential Limitation (GCPL) was performed within the potential range of to 2.5 and 0.005 V (E vs. Li/Li^+) with cycling currents of 37, 74, 372 and 744 mAg^{-1}. Charging and discharging current within one cycle were the same and measured capacities were re-calculated to the amount of SiOC/Sn active mass within the electrodes (85 wt%).

Acknowledgments

This work was financially support by the Deutsche Forschungsgemeinschaft (DFG), Bonn, Germany within SPP1473/JP8, SPP1181 and SFB595 programs. The authors want to acknowledge C. Linck for his support in the sample preparation and assistance in XRD measurements.

Note: The layout of Figure 3 and Table 1 was adjusted after initial online publication.

Received: November 12, 2013
Revised: January 27, 2014
Published online: March 25, 2014

[1] T. Nagaura, K. K. Tozawa, *Prog. Batteries Solar Cells* **1990**, *9*, 209.
[2] T. Nagaura, M. Nagamine, I. Tanabe, N. Miyamoto, *Prog. Batteries Solar Cells* **1989**, *8*, 84.
[3] F. Cheng, J. Liang, Z. Tao, J. Chen, *Adv. Mater. Processes* **2011**, *23*, 1695.
[4] R. Marom, S. F. Amalraj, N. Leifer, D. Jacob, D. Aurbach, *J. Mater. Chem.* **2011**, *21*, 9938.
[5] B. Scrosati, J. Garche, *J. Power Sources* **2010**, *195*, 2419.
[6] H. Kawamoto, *Sci. Technol. Trends* **2010**, *36*, 34.
[7] P. G. Bruce, *Solid State Ionics* **2008**, *179*, 752.
[8] P. G. Bruce, B. Scrosati, J.-M. Tarascon, *Angew. Chem., Int. Ed.* **2008**, *47*, 2930.
[9] A. K. Shukla, T. P. Kumar, *Curr. Sci.* **2008**, *94*, 314.
[10] W.-J. Zhang, *J. Power Sources* **2011**, *196*, 13.
[11] W.-J. Zhang, *J. Power Sources* **2011**, *196*, 877.
[12] C.-M. Park, J.-H. Kim, H. Kim, H.-J. Sohn, *Chem. Soc. Rev.* **2010**, *39*, 3115.
[13] M. N. Obrovac, L. J. Krause, *J. Electrochem. Soc.* **2007**, *154*, A103.
[14] M. Winter, J. O. Besenhard, *Electrochim. Acta* **1999**, *45*, 31.
[15] A. D. W. Todd, P. P. Ferguson, M. D. Fleischauer, J. R. Dahn, *Int. J. Energy Res.* **2010**, *34*, 535.
[16] L. Y. Beaulieu, K. W. Eberman, R. L. Turner, L. J. Krause, J. R. Dahn, *Electrochem. Solid State Lett.* **2001**, *4*, A137.
[17] J. Hassoun, K.-S. Lee, Y.-K. Sun, B. Scrosati, *J. Am. Chem. Soc.* **2011**, *133*, 3139.
[18] Z. Du, S. Zhang, Y. Xing, X. Wu, *J. Power Sources* **2011**, *196*, 9780.
[19] L. Bazin, S. Mitra, P. L. Taberna, P. Poizot, M. Gressier, M. J. Menu, A. Barnabe, P. Simon, J. M. Tarascon, *J. Power Sources* **2009**, *188*, 578.
[20] J. Hassoun, S. Panero, B. Scrosati, *Fuel Cells* **2009**, *9*, 277.
[21] G. Derrien, J. Hassoun, S. Panero, B. Scrosati, *Adv. Mater.* **2007**, *19*, 2336.
[22] J. Kaspar, M. Graczyk-Zajac, R. Riedel, *J. Power Sources* **2013**, *244*, 450.
[23] M. Graczyk-Zajac, L. Toma, C. Fasel, R. Riedel, *Solid State Ionics* **2012**, *225*, 522.
[24] J. Kaspar, M. Graczyk-Zajac, R. Riedel, *Solid State Ionics* **2012**, *225*, 527.
[25] S. Martínez-Crespiera, E. Ionescu, H.-J. Kleebe, R. Riedel, *J. Eur. Ceram. Soc.* **2011**, *31*, 913.
[26] C. Moysan, R. Riedel, R. Harshe, T. Rouxel, F. Augereau, *J. Eur. Ceram. Soc.* **2007**, *27*, 397.
[27] E. Ionescu, C. Terzioglu, C. Linck, J. Kaspar, A. Navrotsky, R. Riedel, *J. Am. Ceram. Soc.* **2013**, *96*, 1899.

[28] E. Ionescu, C. Linck, C. Fasel, M. Müller, H.-J. Kleebe, R. Riedel, *J. Am. Chem. Soc.* **2010**, *93*, 241.
[29] E. Ionescu, B. Papendorf, H.-J. Kleebe, F. Poli, K. Müller, R. Riedel, *J. Am. Chem. Soc.* **2010**, *93*, 1774.
[30] E. Ionescu, B. Papendorf, H.-J. Kleebe, R. Riedel, *J. Am. Chem. Soc.* **2010**, *93*, 1783.
[31] R. Harshe, C. Balan, R. Riedel, *J. Eur. Ceram. Soc.* **2004**, *24*, 3471.
[32] R. Frycek, M. Jelinek, T. Kocourek, P. Fitl, M. Vrnata, V. Myslikk, M. Vrbova, *Thin Solid Films* **2006**, *495*, 308.
[33] N. W. Alcock, V. M. Tracy, T. C. Waddington, *J. Chem. Soc., Dalton Trans.* **1976**, *21*, 2243.
[34] K. Ito, H. J. Bernstein, *Can. J. Chem.* **1956**, *34*, 170.
[35] B. N. S. Bhaktha, C. Kinowski, M. Bouazaoui, B. Capoen, O. Robbe-Cristini, F. Beclin, P. Roussel, M. Ferrari, S. Turrell, *J. Phys. Chem. C* **2009**, *113*, 21555.
[36] N. Dharmaraj, C. H. Kim, K. W. Kim, H. Y. Kim, E. K. Suh, *Spectrochim. Acta, Part A* **2006**, *64*, 136.
[37] S. Samanta, N. K. Mal, A. Manna, A. Bhaumik, *Appl. Catal., A* **2004**, *273*, 157.
[38] T. Ishikawa, Y. Kohtoku, K. Kumagawa, *J. Mater. Sci.* **1998**, *33*, 161.
[39] E. Ionescu, H.-J. Kleebe, R. Riedel, *Chem. Soc. Rev.* **2012**, *41*, 5032.
[40] S. K. Rhee, *J. Am. Ceram. Soc.* **1971**, *54*, 332.
[41] O. Dezellus, N. Eustathopoulos, *J. Mater. Sci.* **2010**, *45*, 4256.
[42] A. Francis, E. Ionescu, C. Fasel, R. Riedel, *Inorg. Chem.* **2009**, *48*, 10078.
[43] S. Dire, F. Babonneau, C. Sanchez, J. Livage, *J. Mater. Chem.* **1992**, *2*, 239.
[44] M. Fukushima, E. Yasuda, Y. Nakamura, Y. Tanabe, *J. Ceram. Soc. Jpn.* **2003**, *111*, 857.
[45] M. Fukushima, E. Yasuda, Y. Nakamura, Y. Teranishi, K. Nakamura, Y. Tanabe, *J. Ceram. Soc. Jpn.* **2004**, *112*, S1531.
[46] S. J. Widgeon, S. Sen, G. Mera, E. Ionescu, R. Riedel, A. Navrotsky, *Chem. Mater.* **2010**, *22*, 6221.
[47] G. D. Soraru, L. Pederiva, J. Latournerie, R. Raj, *J. Am. Chem. Soc.* **2002**, *85*, 2181.
[48] B. Papendorf, K. Nonnenmacher, E. Ionescu, H.-J. Kleebe, R. Riedel, *Small* **2011**, *7*, 970.
[49] M. Graczyk-Zajac, C. Fasel, R. Riedel, *J. Power Sources* **2011**, *196*, 6412.
[50] M. Wilamowska, M. Graczyk-Zajac, R. Riedel, *J. Power Sources* **2013**, *244*, 80.
[51] H. Fukui, H. Ohsuka, T. Hino, K. Kanamura, *J. Power Sources* **2011**, *196*, 371.
[52] P. Kroll, *MRS Online Proc. Library* **2011**, *1313*, 1.
[53] A. Scarmi, G. D. Soraru, R. Raj, *J. Non-Cryst. Solids* **2005**, *351*, 2238.